Quantum Spectroscopy with Undetected Photons for Biomolecular Sensing in the Mid-Infrared: Supplementary Information

Mahya Mohammadi[1,2*], Meryem-Nur Duman[1,2], Isa Ahmadalidokht[1,2], Mohammad Sadraeian[2,3], Christopher G. Poulton[1], Alexander S. Solntsev[1,2], Irina V. Kabakova[1,2*]

[1] *School of Mathematical and Physical Sciences (MaPS), Faculty of Science, University of Technology Sydney, Sydney, NSW 2007, Australia*

[2] *ARC Centre of Excellence in Quantum Biotechnology (QUBIC), University of Technology Sydney, Sydney, NSW 2007, Australia*

[3] *Institute for Biomedical Materials and Devices (IBMD), Faculty of Science, University of Technology Sydney, Sydney, NSW 2007, Australia*

*Correspondence to: Mahya.Mohammadi@student.uts.edu.au, Irina.Kabakova@uts.edu.au

SUPPLEMENTARY NOTE 1: FTIR Measurements

The FTIR spectra used in this work were acquired using a BioATR FTIR instrument, while the QSUP model assumes light transmission through a sample. To relate these two descriptions, the ATR absorbance spectrum was used to estimate the effective absorption coefficient of the sample. In ATR spectroscopy the infrared field interacts with the sample through an evanescent wave with a penetration depth depending on the light wavelength and the refractive indices of the ATR crystal and sample. Using the known refractive index of the ZnSe ATR crystal and the measurement geometry, the average penetration depth in MIR range was estimated to be 100 nm and used to convert the measured ATR absorbance into an absorption coefficient. This coefficient was then used to construct an effective transmissivity amplitude τ for the QSUP model via the Beer–Lambert relation [1]. This approach allows us to compare directly ATR measurements with QSUP numerical simulations.

A. Secondary structure calculations

The negative normalized second derivative of the BSA absorbance at 24 °C, fitted with Gaussian line shape to resolve secondary structure features, is shown in Supplementary Fig. S1 (a). The absorbance is also converted into transmissivity amplitude, which serves as the primary parameter for subsequent analysis in this work. Supplementary Fig. S1 (b) presents the absorbance spectrum of BSA at 24 °C alongside its corresponding transmittance.

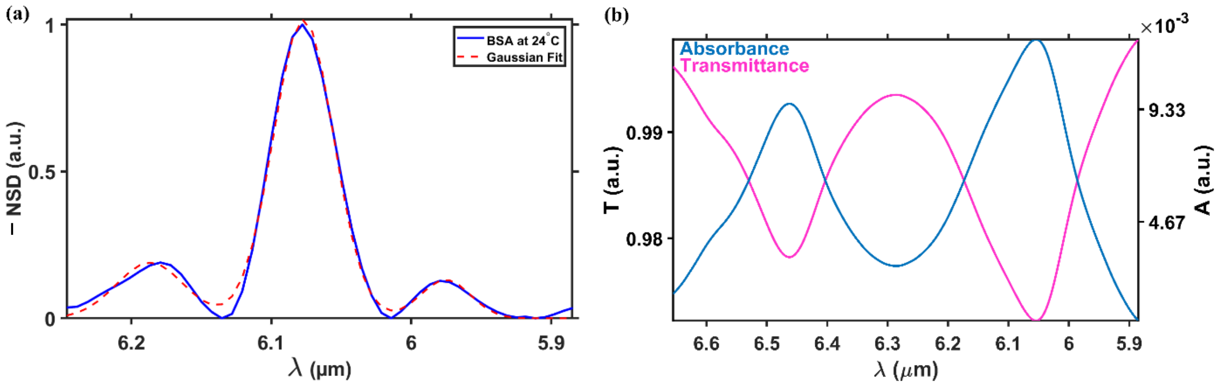

Supplementary Figure S1. **(a)** Analysis of the minus normalized second derivative of BSA absorbance at 24 °C, with Gaussian curve fitting applied to identify secondary structure components. **(b)** Comparison between the absorbance and transmissivity amplitude of BSA at 24 °C

B. Temperature dependent structural changes of BSA

Elevated temperatures are known to induce protein denaturation and alter secondary structure. The amide I band, which contains information on α-helix, β-sheet, β-turn, antiparallel intermolecular β-sheet and random coil [2] is commonly used to analyse and quantify protein secondary structure. In this study, FTIR spectroscopy was used to investigate temperature dependent structural changes in BSA and associated protein dynamics [3].

Our results confirm that the secondary structure of BSA is sensitive to temperature. Figure 3 **(b)** shows the FTIR spectra of BSA at 24 °C and 68 °C, with a clear change at the elevated temperature indicated by the appearance of a shoulder within the amide I region. This spectral feature suggests a redistribution of secondary structure components. Following second derivative analysis and Gaussian curve fitting (see Supplementary Fig. **S**1 (a)), individual bands within the amide I region were assigned (**Table 1**) based on previous studies [4-7]. At 24 °C, the band at 1655 cm^{-1} was attributed to α-helix (~79 %) [4], while the bands at 1627 and 1683 cm^{-1} corresponded to β-sheet (~9%) and β-turn (~13%) [4, 8]. At 68 °C, the α-helix and β-turn content decreased to ~65 % and ~9 % respectively, while β-sheet increased to ~26 %. These changes indicate a temperature dependent transformation of BSA secondary structure, in particular the partial conversion of α-helix and β-turn components into β-sheets and potentially random coils [9], although the latter was not detected in our analysis. Our results are similar with previous reports of heat-induced denaturation of BSA. For example, Zhou et al. [10] observed that at temperatures above 65 °C there was a decrease in α-helix and extended chain structures, and an increase in the relative content of β-sheet structures. This agrees with our observation that secondary structure rearrangements occur only at elevated temperatures.

We did not detect any random coil structures at either temperature, which may be attributed to our assignment of the 1655 cm^{-1} band to α-helix. This interpretation is in good agreement with previous reports where the 1654–1658 cm^{-1} region is assigned to α-helices [4, 11], however, there have been inconsistencies in literature regarding the frequency assignment for α-helix. Some researchers attribute the frequency of 1660 cm^{-1} to random coil structures [9, 12], whereas others suggest that α-helix and random coil overlap within the same absorption band frequency [9, 13], resulting in ambiguity in their distinction.

The band at 1627 cm^{-1} was assigned based on literature [14], where H_2O was commonly used as the solvent. Although PBS was used in our study, after solvent subtraction, the spectra should not differ substantially [15]. Dong et al. [4] assigned bands in the region of 1624–1642 cm^{-1} to β-sheets. However, the assignment of the band around 1630 cm^{-1} has been under controversy in literature. While it is frequently attributed to intramolecular β-sheet structures [14, 16-18], several studies propose that it arises from short segment chains connecting α-helix segments [19, 20]. Given that the secondary structure of BSA consists of approximately 67% helix, 10% turn and 23% extended chain, and that x-ray crystallographic studies of HSA have revealed no β-sheet content [21-23], the interpretation of the 1630 cm^{-1} band remains uncertain.

SUPPLEMENTARY NOTE 2: QSUP Simulation

The SPDC intensity of signal photons in our simulation is given by equation (3) in the main text with δ_s as

$$\delta_s = \delta_a + \delta_b + \delta_m \tag{S1}$$

with

$$\delta_a(\lambda_s, \theta_s) = \left(k_{p,a} - k_{s,a}\cos\theta_{s,a} - k_{i,a}\cos\theta_{i,a}\right)L_a \, , \tag{S2}$$

$$\delta_b(\lambda_s, \theta_s) = \left(k_{p,b} - k_{s,b}\cos\theta_{s,b} - k_{i,b}\cos\theta_{i,b}\right)L_b \, , \tag{S3}$$

$$\delta_m(\lambda_s, \theta_s) = \left(k_{p,m} - k_{s,m}\cos\theta_{s,m} - k_{i,m}\cos\theta_{i,m}\right)L_m \, . \tag{S4}$$

Here δ_m, δ_b and δ_a are the longitudinal phase mismatch in the nonlinear crystal, including contributions from the sample, the biocell and air gap. The quantities $k_{\{p,s,i\},\{a,b,m\}}$ are the wavenumbers of the pump, signal and idler in the air gap, biocell, and material sample, with $\theta_{\{p,s,i\},\{a,b,m\}}$ denoting their corresponding propagation angles. Some parameters are fixed according to the specifications of the instruments we use. For example, L_b=10 mm is determined by the thickness of the CaF_2 windows in the biocell (the biosample holder) where each window has a thickness of 5 mm. However, several parameters influence the efficiency, fringe visibility, and fringe position on the camera/screen. The most critical parameters include the length of the nonlinear crystal, the sample optical path length, and the distance between the nonlinear crystal and the parabolic mirror (air gap in simulation). Understanding the role of each parameter is essential for optimizing experimental performance. Based on the simulated visibility, key experimental parameters are carefully chosen.

A. The effect of nonlinear crystal length

The nonlinear crystal length L controls both the SPDC efficiency and the phase-matching bandwidth. As discussed in the main text, this introduces a trade-off between photon-pair generation efficiency and interference visibility.

Numerical simulations were performed for a range of crystal lengths, and L=5 mm was identified as an optimal value, providing a balance between photon flux and fringe visibility.

The visibility V obtained from the QSUP model and the transmissivity τ derived from FTIR are not intrinsically equal, as they originate from different measurement approaches. Their comparison is made under the assumption of equivalent sensitivity to absorption, such that variations in τ correspond to variations in V (see Supplementary Fig. S2).

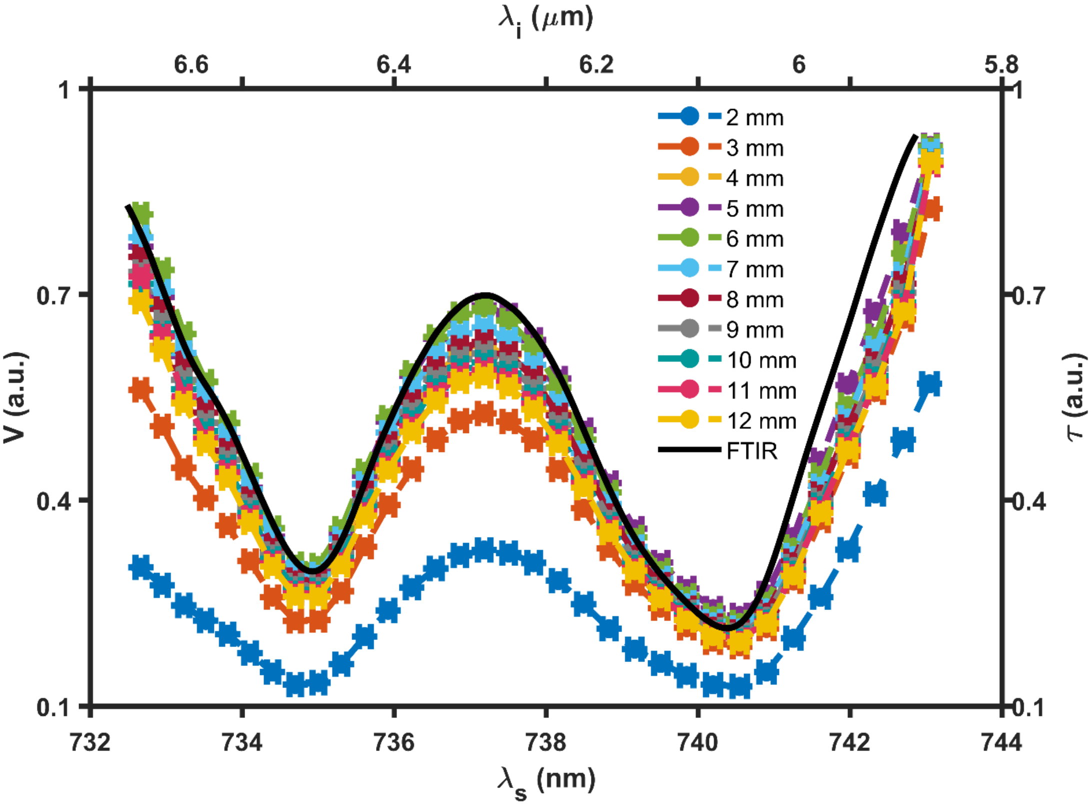

Supplementary Figure S2. The effect of different nonlinear-crystal lengths on visibility. L=5 mm is identified as optimal for this numerical experiment.

B. The effect of sample optical path length

The sample length L_m determines the optical path length and thus the interaction strength between the idler photon and the sample. As discussed in the main text, this leads to a trade-off between absorption and interferometric visibility.

Simulations indicate that the sample optical path length 6–8 µm provides near-optimal performance, with 6 µm selected to minimise sample volume. This corresponds to a sample volume of approximately 10 µL in a standard CaF2 biocell, which is smaller than that typically required for conventional FTIR measurements.

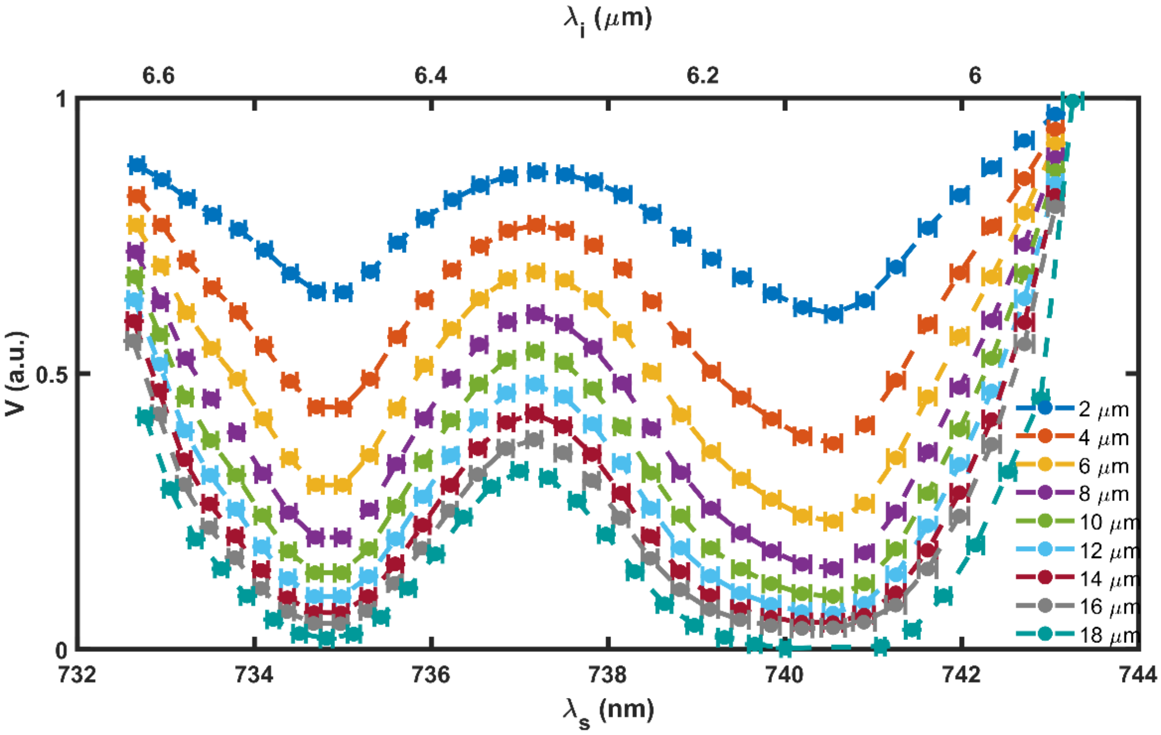

Supplementary Figure S3. The effect of different values of the sample lengths on visibility. L_m= 6–8 µm is identified as optimal for this numerical experiment.

C. The effect of Crystal-to-OAPM Distance

The crystal–mirror separation L_a controls the phase difference between the two SPDC passes and therefore the spectral position of the interference fringes (see main text). Simulations show that $L_a = -8.75$ mm provides optimal fringe alignment across the Amide I–II region, maximising spectral contrast.

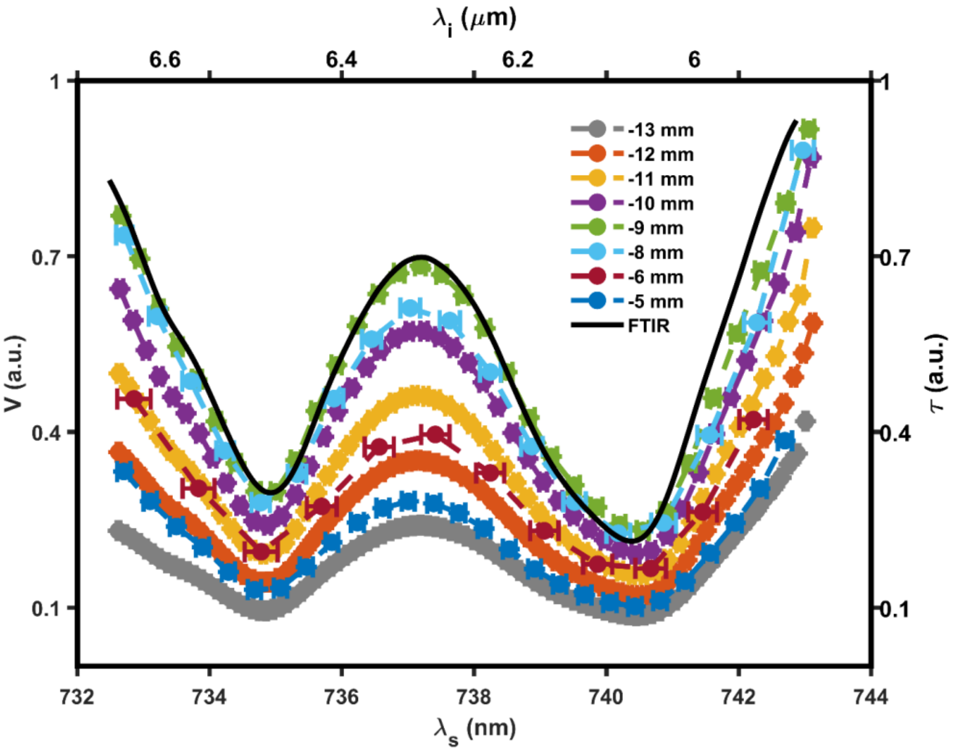

Supplementary Figure S4. The effect of various values of Crystal-to-OAPM Distance

However, the analysis also reveals that not all values of $\mathrm{L_a}$ are suitable for reliable measurements. In particular, around $\mathrm{L_a} \approx -7\mathrm{mm}$, the interferometric visibility approaches zero. This behaviour can be observed in the fringe pattern as illustrated in Supplementary Fig. S5. For $\mathrm{L_a} = -7\mathrm{mm}$, shown in Supplementary Fig. S5 (a) the phase map of $\cos(\delta + \delta_a + \delta_b + \delta_m)$ shows strongly curved fringes that run almost parallel to the line given by phase matching in the crystal (black line in Supplementary Fig. S5 (a)). In contrast, for $\mathrm{L_a} = -9\mathrm{mm}$ the phase fringes become nearly vertical, and the black line clearly crosses the fringes (see Supplementary Fig. S5 (b)).

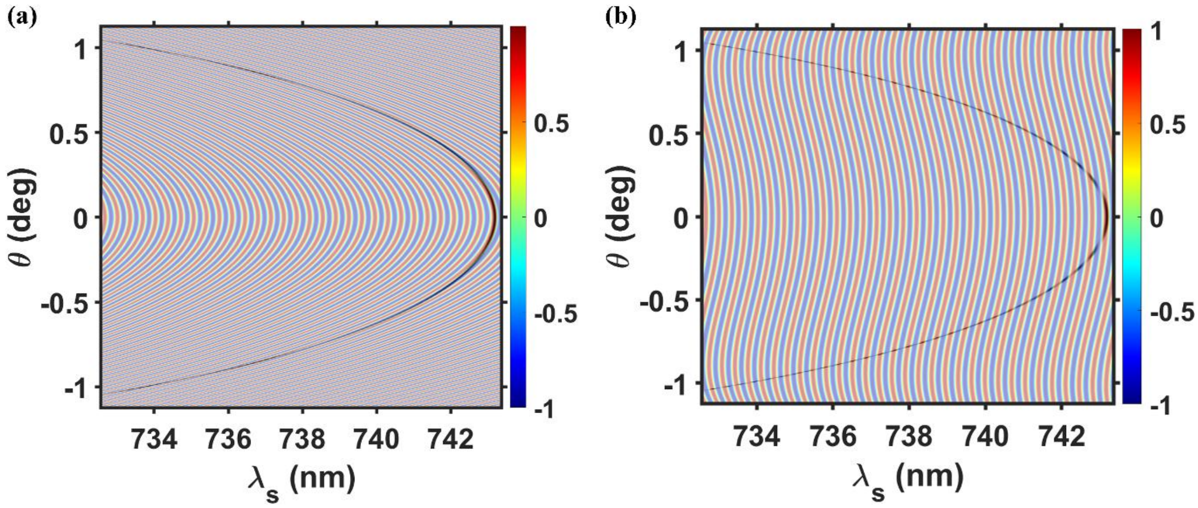

Supplementary Figure S5. Effect of crystal–mirror distance on interference fringes. Overlay of $\cos(\delta + \delta_a + \delta_b + \delta_m)$ with the angular–wavelength spectrum showing the change in fringe angular dependence. **(a)** $\mathrm{L_a} = -7$ mm, where the visibility is suppressed. **(b)** $\mathrm{L_a} = -8.75$ mm, where clear high-contrast fringes are observed.

The fringe visibility will shrink to exactly zero when the function describing the fringes $\cos(\delta + \delta_a + \delta_b + \delta_m)$ is constant along the line $\delta = 0$ in the (λ_s, θ_s) plane. This situation corresponds to the case where the phase accumulated along the various parts of the NL crystal, material, biocell and air gap cancel exactly along the optical path. An approximation for when this occurs can be obtained under the assumption that the transverse wavenumbers are small. For convenience, we define the transverse wavenumber as

$$q = k_s \sin\theta_s \ . \tag{S5}$$

From Equations (S2-S4), and noting that the transverse wavevector is conserved across each section, we have the following for the individual phases across the air gap, biocell and sample:

$$\delta_a = \left(k_{p,a} - \sqrt{k_{s,a}^2 - q^2} - \sqrt{k_{i,a}^2 - q^2}\right) L_a \, , \tag{S6}$$

$$\delta_b = \left(k_{p,b} - \sqrt{k_{s,b}^2 - q^2} - \sqrt{k_{i,b}^2 - q^2}\right) L_b \, , \tag{S7}$$

$$\delta_m = \left(k_{p,m} - \sqrt{k_{s,m}^2 - q^2} - \sqrt{k_{i,m}^2 - q^2}\right) L_m \, . \tag{S8}$$

The length of the sample material is typically much smaller than that of both the air gap and the biocell, being on the scale of microns as opposed to cm, i.e. $L_m \ll L_a, L_b$; for the purpose of examining the visibility of the fringes the phase accumulated across the sample can therefore be neglected. We furthermore now assume that all angles involved remain small on the phase-matching line $\delta = 0$, such that $q \ll k_s, k_i$ in both the air gap and the biocell. We can then expand the total phase change as:

$$\begin{aligned}\delta + \delta_a + \delta_b + \delta_m \approx & \left[k_{p,a} - k_{s,a} - k_{i,a} + \frac{q^2}{2}\left(\frac{1}{k_{s,a}} + \frac{1}{k_{i,a}}\right)\right] L_a \\ & + \left[k_{p,b} - k_{s,b} - k_{i,a} + \frac{q^2}{2}\left(\frac{1}{k_{s,b}} + \frac{1}{k_{i,b}}\right)\right] L_b \, .\end{aligned} \tag{S9}$$

Because of energy conservation in the SPDC process in the NL crystal we have

$$\frac{k_p}{n_p} - \frac{k_s}{n_s} - \frac{k_i}{n_i} = 0 \, , \tag{S10}$$

where n_p, n_s and n_i are the refractive indices of the NL crystal at the signal, pump and idler wavelengths respectively. Using this relation we find that $k_{p,a} - k_{s,a} - k_{i,a} = n_a\left(\frac{k_p}{n_p} - \frac{k_s}{n_s} - \frac{k_i}{n_i}\right) = 0$, and $k_{p,b} - k_{s,b} - k_{i,b} = n_a\left(\frac{k_p}{n_p} - \frac{k_s}{n_s} - \frac{k_i}{n_i}\right) = 0$ where n_a is the refractive index of the gap and n_b is the refractive index of the biocell, both assumed to be approximately constant across the entire wavelength range. We then have the total phase accumulation:

$$\delta + \delta_a + \delta_b + \delta_m \approx \frac{q^2}{2}\left(\frac{1}{k_{s,a}} + \frac{1}{k_{i,a}}\right)L_a + \frac{q^2}{2}\left(\frac{1}{k_{s,b}} + \frac{1}{k_{i,b}}\right)L_b$$

$$\approx \left(\frac{n_s}{k_s} + \frac{n_i}{k_i}\right)\left(\frac{L_a}{n_a} + \frac{L_b}{n_b}\right) \quad . \qquad \text{(S11)}$$

The total phase is therefore constant, across all wavelengths and to fourth order in q, provided

$$\left(\frac{L_a}{n_a} + \frac{L_b}{n_b}\right) = 0 \qquad \text{(S12)}$$

that is, for air gap lengths given by

$$L_a^{\min} \approx -\frac{n_a}{n_b}L_b \qquad \text{(S13)}$$

This is an approximate condition for the point near which the visibility of the fringes exactly vanishes over the entire wavelength range. The exact value of L_a where the fringe visibility disappears may change if the angles θ_s and θ_i become larger, or if the sample length L_m approaches the scale of the air gap and biocell.

SUPPLEMENTARY REFERENCES

1. Mayerhöfer, T. G., Pahlow, S. & Popp, J. The Bouguer–Beer–Lambert law: shining light on the obscure. *ChemPhysChem* **21**, 2029–2046 (2020).
2. Zhang, J. & Yan, Y.-B. Probing conformational changes of proteins by quantitative second-derivative infrared spectroscopy. *Anal. Biochem.* **340**, 89–98 (2005).
3. Yuan, B., Murayama, K. & Yan, H. Study of thermal dynamics of defatted bovine serum albumin in D_2O Solution by Fourier transform infrared spectra and evolving factor analysis. *Appl. Spectrosc.* **61**, 921–927 (2007).
4. Dong, A., Huang, P. & Caughey, W. S. Protein secondary structures in water from second-derivative amide I infrared spectra. *Biochemistry* **29**, 3303–3308 (1990).
5. Kalnin, N. N., Baikalov, I. A. & Venyaminov, S. Yu. Quantitative IR spectrophotometry of peptide compounds in water (H_2O) solutions. III. Estimation of the protein secondary structure. *Biopolymers* **30**, 1273–1280 (1990).
6. Venyaminov, S. Yu. & Kalnin, N. N. Quantitative IR spectrophotometry of peptide compounds in water (H_2O) solutions. I. Spectral parameters of amino acid residue absorption bands. *Biopolymers* **30**, 1243–1257 (1990).
7. Venyaminov, S. Yu. & Kalnin, N. N. Quantitative IR spectrophotometry of peptide compounds in water (H_2O) solutions. II. Amide absorption bands of polypeptides and fibrous proteins in α-, β-, and random coil conformations. *Biopolymers* **30**, 1259–1271 (1990).
8. Chou, P. Y. & Fasman, G. D. β-turns in proteins. *J. Mol. Biol.* **115**, 135–175 (1977).
9. Usoltsev, D., Sitnikova, V., Kajava, A. & Uspenskaya, M. Systematic FTIR spectroscopy study of the secondary structure changes in human serum albumin under various denaturation conditions. *Biomolecules* **9**, 359 (2019).
10. Zhou, X., He, Z. & Huang, H. Secondary structure transitions of Bovine serum albumin induced by temperature variation. *Vib. Spectrosc.* **92**, 273–279 (2017).

11. Holloway, P. W. & Mantsch, H. H. Structure of cytochrome b5 in solution by Fourier-transform infrared spectroscopy. *Biochemistry* **28**, 931–935 (1989).

12. Olsztyska-Janus, S., Gsior-Gogowska, M., Szymborska-Maek, K., Czarnik-Matusewicz, B. & Komorowsk, M. Specific applications of vibrational spectroscopy in biomedical engineering. In *Biomedical Engineering, Trends, Research and Technologies* (InTech, 2011).

13. Srour, B., Bruechert, S., Andrade, S. L. A. & Hellwig, P. Secondary structure determination by means of ATR-FTIR spectroscopy. *Methods Mol. Biol.* **1635**, 195–203 (2017).

14. Casal, H. L., Köhler, U. & Mantsch, H. H. Structural and conformational changes of β-lactoglobulin B: an infrared spectroscopic study of the effect of pH and temperature. *Biochim. Biophys. Acta* **957**, 11–20 (1988).

15. Grdadolnik, J. Infrared difference spectroscopy. *Vib. Spectrosc.* **31**, 279–288 (2003).

16. Bauelos, S., Arrondo, J. L. R., Goi, F. M. & Pifat, G. Surface-core relationships in human low density lipoprotein as studied by infrared spectroscopy. *J. Biol. Chem.* **270**, 9192–9196 (1995).

17. Bañuelos, S. & Muga, A. Structural requirements for the association of native and partially folded conformations of α-lactalbumin with model membranes. *Biochemistry* **35**, 3892–3898 (1996).

18. Reinstädler, D., Fabian, H., Backmann, J. & Naumann, D. Refolding of thermally and urea-denatured ribonuclease a monitored by time-resolved FTIR spectroscopy. *Biochemistry* **35**, 15822–15830 (1996).

19. Reisdorf, , William C. & Krimm, S. Infrared amide I band of the coiled coil. *Biochemistry* **35**, 1383–1386 (1996).

20. Gilmanshin, R., Williams, S., Callender, R. H., Woodruff, W. H. & Dyer, R. B. Fast events in protein folding: Relaxation dynamics of secondary and tertiary structure in native apomyoglobin. *Proc. Natl Acad. Sci.* **94**, 3709–3713 (1997).

21. Reed, R. G., Feldhoff, R. C., Clute, O. L. & Peters, T. Fragments of bovine serum albumin produced by limited proteolysis: conformation and ligand binding. *Biochemistry* **14**, 4578–4583 (1975).

22. WETZEL, R. *et al.* Temperature behaviour of human serum albumin. *Eur. J. Biochem.* **104**, 469–478 (1980).

23. Carter, D. C. & Ho, J. X. Structure of serum albumin. *Advances in Protein Chemistry* **45**, 153–203 (1994).